Label-free cellular manipulation and sorting via biocompatible ferrofluids

Ayse R. Kose[a], Birgit Fischer[b], Leidong Mao[c], and Hur Koser[a,1]

[a]Department of Electrical Engineering, School of Engineering and Applied Sciences, Yale University, New Haven, CT 06520-8284; [b]Hamburger Synchrotronstrahlungslabor, Deutsches Elektronen Synchrotron, Notkestrasse 85, 22607 Hamburg, Germany; and [c]Faculty of Engineering, Nanoscale Science and Engineering Center, University of Georgia, Athens, GA 30602

Communicated by Paul A. Fleury, Yale University, New Haven, CT, October 23, 2009 (received for review June 7, 2009)

We present a simple microfluidic platform that uses biocompatible ferrofluids for the controlled manipulation and rapid separation of both microparticles and live cells. This low-cost platform exploits differences in particle size, shape, and elasticity to achieve rapid and efficient separation. Using microspheres, we demonstrate size-based separation with 99% separation efficiency and sub-10-μm resolution in <45 s. We also show continuous manipulation and shape-based separation of live red blood cells from sickle cells and bacteria. These initial demonstrations reveal the potential of ferromicrofluidics in significantly reducing incubation times and increasing diagnostic sensitivity in cellular assays through rapid separation and delivery of target cells to sensor arrays.

ferromicrofluidics | magnetic hole | cell separation

Early diagnosis of diseases involving rare cells in blood (such as metastatic cancer or low-level bacteremia) and accurate monitoring of certain genetic conditions (such as sickle cell anemia) require rapid and accurate separation, sorting, and direction of target cell types toward a sensor surface. In that regard, cellular manipulation, separation, and sorting are increasingly finding application potential within various bioassays in the context of cancer diagnosis (1), pathogen detection (2), and genomic testing (3, 4). A variety of contactless micromanipulation methods exist, including optical tweezers (5, 6), dielectrophoresis (DEP) (7), magnetic bead-based separators (8, 9), and deterministic hydrodynamics (10). However, most existing methods have been unable to reliably achieve fast speed, high throughput and resolution, and low cost simultaneously (11–13). Optical tweezers offer high resolution and sensitivity for manipulating single cells, although such manipulation may cause sample heating (14) and is typically limited to a very small area (15). Holographic schemes have recently extended the reach of optical tweezers to several tens of cells simultaneously (16), although the overall throughput remains quite low. Schemes based on electric fields, e.g., DEP, offer the potential to realize integrated, cost-effective devices for the simultaneous manipulation of multiple cells; nevertheless, their performance depends sensitively on the electrical properties of the specific liquid medium, the particle shape, and its effective dielectric constant (17). DEP device operating regimes and the working ionic medium need to be carefully optimized for each different cell type so as to reach a workable compromise between the need to reduce heating (18, 19) and minimize cell polarization (20). Using functionalized magnetic beads to separate target molecules and cells overcomes these challenges through the use of magnetic fields instead of electric. The downside of this technique is the lengthy incubation times and wash cycles and the difficulty of removing the label post priori (21). The deterministic hydrodynamics approach, as demonstrated by Davis et al. (10), is capable of achieving high resolution of separation without the use of any electromagnetic fields. However, high throughput with this device requires high-resolution lithography on a large area, keeping the cost per device high.

To address these limitations, we have developed a microfluidic platform based on ferrohydrodynamics for the label-free manipulation and separation of cells and microorganisms within biocompatible ferrofluids. Our technique uses a water-based ferrofluid as a uniform magnetic environment that surrounds the cells within a microfluidic channel. Cells and other nonmagnetic particles within the ferrofluid act as "magnetic voids" (22), in a manner analogous to electronic holes in a semiconductor. An externally applied magnetic field gradient attracts magnetic nanoparticles, which causes nonmagnetic microparticles or cells to be effectively pushed away (23, 24). Recently, this principle has been applied to capture nonmagnetic microbeads between magnetic film islands in a microchannel filled with ferrofluid (25). In contrast, our approach uses a microfluidic device with integrated copper electrodes that carry currents to generate programmable magnetic field gradients locally (26) (Fig. 1*A*; see *SI Appendix* for device fabrication details). This device is constructed on an inexpensive printed circuit board that features an insulated copper layer etched via a single, low-resolution transparency mask to define the electrodes. The microfluidic channel is constructed via soft lithography using a low-resolution mold. Overall, device fabrication does not even necessitate a clean room, and hence, is extremely simple, rapid, and inexpensive.

Alternating currents up to 7 A peak to peak in amplitude and with frequencies from 10 Hz to 100 kHz (corresponding to a maximum magnetic field strength of 90 Oe within the ferrofluid) are applied to the electrodes in quadrature to create a periodic magnetic field pattern that travels along the length of the microchannel. With this configuration, the device is able to create both magnetic field gradients, resulting in a time-average force on the cells, and local rotation of ferrofluid magnetization, which eventually results in torque on the nonmagnetic particles (Fig. 1*B*; see Movie S1). When the current is turned on, the cells are rapidly pushed away from the electrodes to the top of the channel (because of magnetic force), where they start to rotate and roll along its length (because of magnetic torque). The device behavior mimics the frequency-dependent susceptibility of the particular ferrofluid used (see *SI Appendix* for force and torque derivation). For a given particle size, its speed depends on the local force and torque values along the channel length (Fig. 1*C*). At low frequencies, the force dominates, pushing the nonmagnetic microparticles up to the channel ceiling and into the space between the electrodes; at high frequencies, the rolling microparticles can overcome the diminishing repulsion caused by magnetic force and move continuously along the channel (Fig. 1*D*). Using this microfluidic setup, the typical magnetic force

Author contributions: H.K. designed research; A.R.K. performed research; B.F. and L.M. contributed new reagents/analytic tools; A.R.K. and H.K. analyzed data; A.R.K. and H.K. wrote the paper; B.F. developed ferrofluid synthesis protocols; L.M. developed circuitry and fabrication protocols; and H.K. developed theoretical and analytical background.

The authors declare no conflict of interest.

[1]To whom correspondence should be addressed. E-mail: hur.koser@yale.edu.

This article contains supporting information online at www.pnas.org/cgi/content/full/0912138106/DCSupplemental.

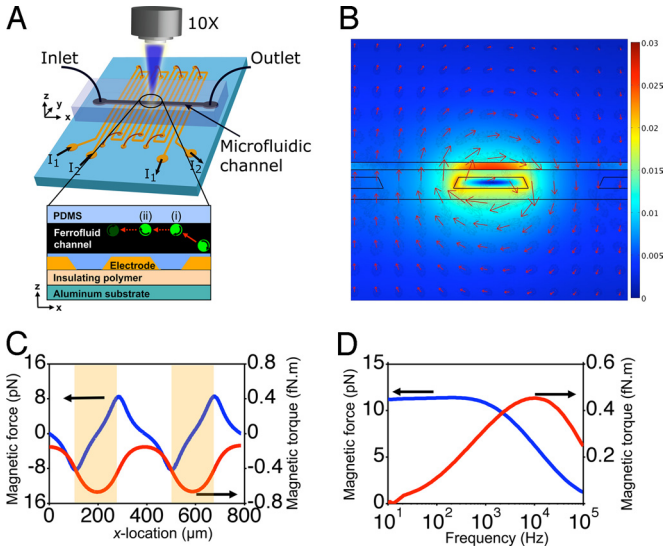

Fig. 1. Ferromicrofluidic device and particle manipulation platform. (*A*) Schematic of the experimental setup displaying the microfluidic channel and the underlying electrodes (not drawn to scale). Two output channels from an amplifier provide sinusoidal currents (I_1 and I_2) phase-locked 90° with respect to each other. The neighboring electrodes on the substrate are connected in a manner to carry sinusoidal currents in quadrature and support a traveling-wave magnetic field within the microfluidic channel. The magnetic field gradient generated pushes the nonmagnetic microspheres or cells within the ferromicrofluidic channel up and into the gap between electrodes (*i*); the traveling field also causes the cells to rotate and roll along the channel ceiling, resulting in continuous translation along the length of the channel at frequencies above a threshold (*ii*). The resulting microparticle motion is observed with an upright microscope from above and captured with a CCD camera at 18 frames per s for further analysis. (*B*) COMSOL simulation of magnetic field (dark arrows) and magnitude of magnetic flux density (color) across the cross-section of the ferromicrofluidic device at a given instant in time. Fainter arrows depict the field at every 30° within one period. Simulation is for 12-A peak-to-peak current input at 1,670 Hz. (*C*) Computed force and torque on a 6-μm diameter microsphere along the length of the microchannel with 7-A peak-to-peak input excitation at 4.6 kHz. (*D*) Computed magnetic force and torque as a function of frequency for the same particle located between electrodes on the channel ceiling. Input current amplitude is 7 A peak to peak; assumed slip factor for all simulations depicted here is 1.

that can be applied on a particle several micrometers in diameter is on the order of tens of piconewtons, significantly larger than what is typical with optical tweezers on μm-size particles. This actuation force can be increased by applying larger excitation currents; a simple heat sink maintains the channel contents at room temperature up to 10-A peak-to-peak input current (27).

Ferrofluid Properties and Device Characterization

Most common applications of ferrofluids in biomedicine involve highly dilute colloidal suspensions of magnetic nanoparticles. Their widest commercial use is as MRI contrast agents (28). When properly coated with targeting antibodies, they can also be used in hyperthermia therapy for cancer or as sensors to detect pathogens (29).

Using highly concentrated ferrofluids with live cells has traditionally proven to be a challenge, because it requires a carefully engineered colloidal system. The ferrofluid parameters that are most relevant to sustaining live cells include pH, ionic strength, and nanoparticle–surfactant combination, together with their overall and relative concentrations. Finding the right nanoparticle–surfactant combination is crucial in this regard: the ferrofluid needs to be stable at a pH of 7.4, and colloidal stability has to be maintained up to an ionic strength that can sustain live cells. One also needs to pay special attention to the size distribution of the nanoparticles within the ferrofluid. If there exist nanoparticles only a few nanometers in diameter, they could pass through the cell membrane and cause direct cytotoxicity (29). For this reason, the magnetic precipitation step adopted in our ferrofluid synthesis protocol is specifically designed to leave the smallest nanoparticles behind.

Traditional approaches to improving ferrofluid biocompatibility typically involve covering the magnetic nanoparticles permanently with a thick polymer layer [such as dextran (30)], because the surfactant molecules reduce toxicity by impeding direct contact with the surface of the inorganic nanoparticles. However, such an approach leads to a significant reduction in the volume content of the magnetic nanoparticles within the ferrofluid and a corresponding decline in its susceptibility. Higher ferrofluid susceptibility typically translates to faster particle manipulation, so we have chosen to optimize our ferrofluid by using a short surfactant molecule.

The ferrofluid used in our experiments comprised cobalt-ferrite nanoparticles suspended in water and stabilized with citrate (31) (see *SI Appendix* for ferrofluid synthesis details). Mean nanoparticle core diameter within the ferrofluid, as determined with transmission electron microscopy (TEM), was found to be 11.3 ± 4.4 nm (Fig. 2*A*). From simultaneous fits to ac susceptibility and dc magnetization data (Fig. 2*B*; see *SI Appendix* for more details), the average hydrodynamic diameter was determined to be 72.5 nm. The discrepancy between the average hydrodynamic diameter and the individual core sizes observed in TEM images points to a certain degree of particle aggregation within the colloidal suspension of the ferrofluid. This finding was also confirmed through dynamic light scattering measurements, which yielded an average hydrodynamic diameter of 64.9 nm on highly diluted samples of ferrofluid (see *SI Appendix*). Nevertheless, compared with the μm-sized microspheres and cells, the magnetic nanoparticles were still small enough to approximate the ferrofluid as a continuous magnetic medium.

During synthesis, we determined that the optimum ionic concentration within the ferrofluid to provide a good compromise between cell viability (as determined by the trypan blue test; see *SI Appendix*) and ferrofluid stability was 40 mM (Fig. 2*C*). During the course of a given experiment, cells retained their viability. We observed that 75% of cells remained viable, even after being suspended in the ferrofluid for several hours, enabling extended tests involving live cell manipulation and separation.

Before the cell manipulation experiments, we characterized our ferromicrofluidic devices by using fluorescent polystyrene microspheres (Duke Scientific; monodisperse sets with diameters ranging from 1.2 to 9.9 μm). To understand the influence of excitation frequency and current amplitude on the behavior of nonmagnetic microparticles dispersed in ferrofluid, we performed a series of experiments using different sizes of microspheres at various excitation frequencies and current amplitudes. Microspheres of a given size were mixed with the ferrofluid in small quantities (up to 1.1×10^6 microspheres per mL for the smallest microparticle diameter) and subsequently added to the microfluidic channel. The channel inlet and outlet were clamped at both ends to prevent transient fluid motion. Microspheres near the roof of the microchannel were imaged from above with an upright fluorescent microscope (Zeiss AxioImager A1) and a high-sensitivity video camera (Retiga 2000R) using StreamPix software. Image analysis was performed offline in MATLAB (MathWorks) via an optical flow algorithm. The program could automatically track the trajectory and determine the size of thousands of individual microspheres within the field of view in <1 min.

During our experiments, two types of particle dynamics were observed. At low frequencies, the microspheres localized be-

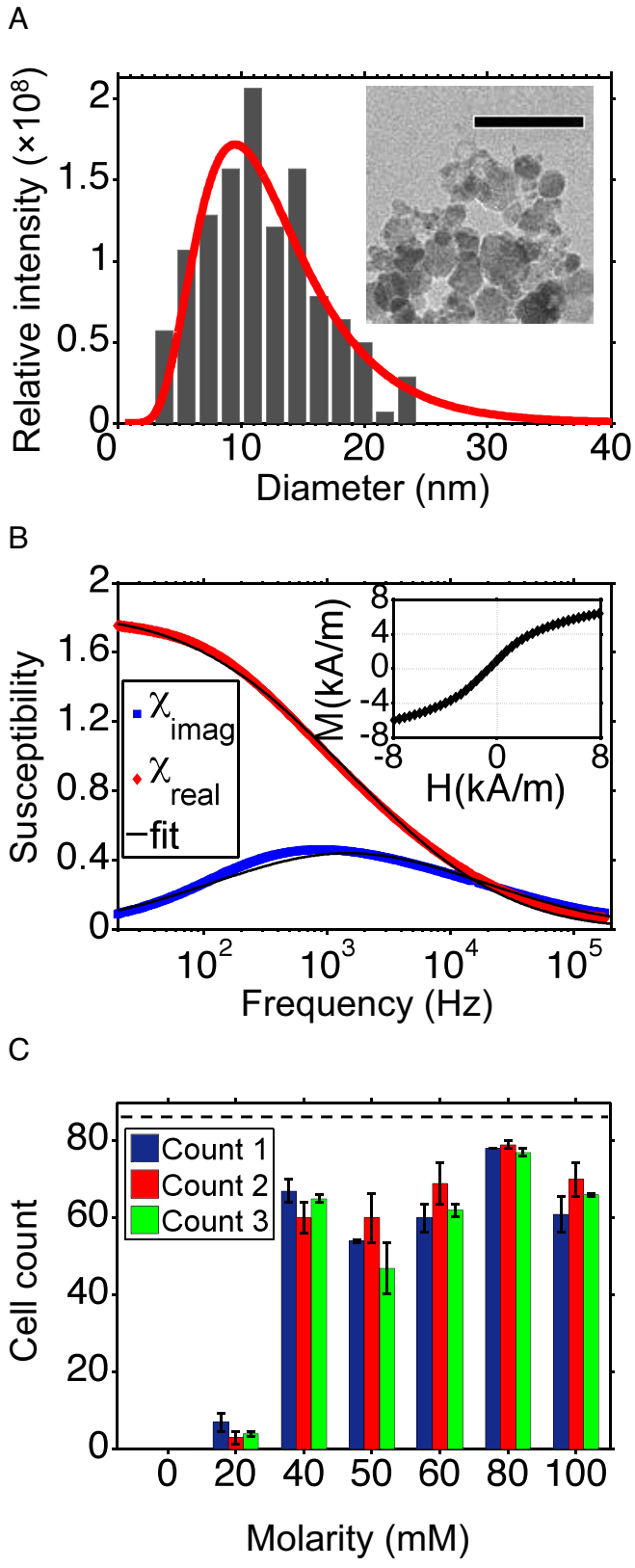

Fig. 2. Biocompatible ferrofluid characterization. (*A*) Distribution of cobalt-ferrite nanoparticle sizes within the ferrofluid, as obtained by TEM. Mean nanoparticle core diameter is 11.3 ± 4.4 nm. (Scale bar: 50 nm.) (*B*) ac susceptibility and dc magnetization curve (*Inset*) of the ferrofluid. A fit to the ac susceptibility data assuming a log-normal size distribution indicates moderate particle aggregation with a mean hydrodynamic diameter of 72.5 nm. (*C*) Live cell count vs. citrate concentration. For our experiments, 40 mM citrate concentration (stabilized with citric acid to yield a pH of 7.4) is found to be optimum for cell viability and ferrofluid stability combined. The dashed line shows the cell count in the original blood sample. Count 3 corresponds to cells spending ≈1 h in the citrate solution.

tween the electrodes, where repulsive forces caused by magnetic field gradients form local minima (Fig. 3*A* and Movie S2). Frequencies above a critical value, f_c, led to continuous translation of the microspheres along the length of the channel roof (Movie S3); this critical frequency depended only on particle size and electrode spacing, not on input current amplitude (Fig. 3*B*). The average velocity of microspheres of a given size depended on the excitation frequency, current amplitude, and their location with respect to the underlying electrodes.

In experiments with various microsphere diameters, we found a monotonic increase in critical frequency with increasing particle size (Fig. 4*A*), demonstrating the potential for size-based particle separation through excitation frequency control. This phenomenon may be explained through a simple hydrodynamic reasoning. Both magnetic force and torque scale with particle volume (R^3); the hydrodynamic drag that resists linear particle motion scales with R against force and R^2 against torque that rolls the particle. Hence, linear particle velocity caused by magnetic force alone depends on R^2, whereas that caused by torque scales with R (see *SI Appendix* for details). This observation indicates that torque effects on smaller particles are relatively more significant and explains why smaller microparticles can overcome the repulsion of magnetic force traps and propagate continuously within the channel at lower frequencies. The solid curve depicted in Fig. 4*A* represents simulation results for critical frequency and explains the data very well for an average microsphere-wall gap of ≈1 nm and no-slip conditions applied to the rotation of the microspheres (see *SI Appendix*).

Fig. 4*B* shows the average velocity of 2.2- and 9.9-μm microspheres (mixed in an 8:1 ratio within the same ferrofluid) under excitation frequencies ranging from 10 Hz to 100 kHz. For a wide frequency range, the smaller particles translated continuously, whereas the larger particles were trapped between the electrodes. In this particular experiment and others, a mixture of particles/cells was eventually separated into two groups, e.g., those trapped vs. those cleared from channel. Assuming that the target particles/cells are those that are intended for trapping, we define the trapping efficiency as the ratio of the number of target moieties within the trapped group to their corresponding number in the initial mixture. Similarly, separation efficiency is defined as the ratio of the number of nontarget moieties within the cleared group to their corresponding number in the initial mixture. However, particle/cell purity is simply the ratio of the number of target cells within the trapped group to the total number of cells in that group. At an excitation frequency of 400 Hz, 96.5% of the 9.9-μm microspheres (167 of 173) were trapped within 10 s, whereas the 2.2-μm particles (1,285 of 1,294) continued to translate along the channel and were cleared out of the observation window (45 s) without being trapped (Fig. 4 *C* and *D* and Movie S4) with a 99.3% separation efficiency. The particle purity in the trapped group was 94.9% (167 targets of 176 total trapped particles). We note that most of the small microspheres that failed to clear the channel were stuck on the polydimethylsiloxane (PDMS) wall in random locations, instead of being trapped between the electrodes. With better channel preparation, the separation efficiency and particle purity could be even higher.

Particle motion was also determined to depend on electrode spacing, with a smaller spacing leading to faster microsphere travel and a reduction in critical frequency (Fig. S1*B*). This phenomenon may be used in a device featuring regions of electrodes with different gaps to use the same excitation fre-

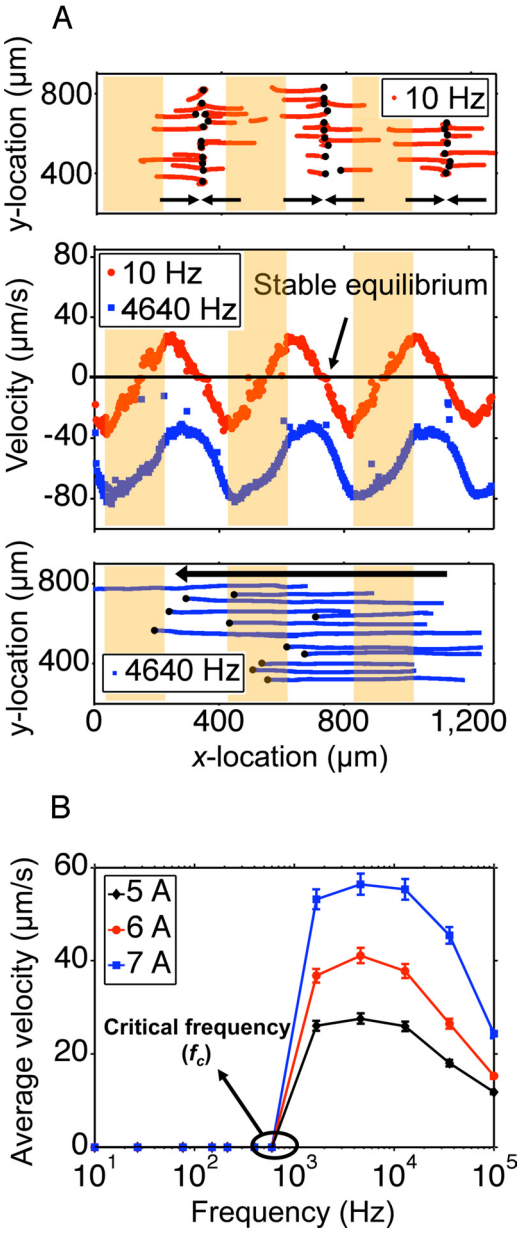

Fig. 3. Particle velocity as a function of input frequency and current amplitude. (*A*) (*Middle*) Spatial distribution of instantaneous average *x*-velocities for 6-μm-diameter particles at 7-A input current amplitude (peak to peak) at two different frequencies. Because of repulsive forces from magnetic field gradients, microparticles either slow down or completely stop in between electrodes. Zero crossings with negative slope correspond to stable equilibrium points (i.e., particle trapping). (*Top*) At 10 Hz, particle trajectories terminate in between electrodes, resulting in trapping. (*Bottom*) At 4,640 Hz, particles move continuously throughout the length of the channel. This is the regime where magnetic torque from the locally rotating component of the traveling wave dominates over the repulsive forces. The black dots at the end of each trajectory indicate where particles eventually stop. (*B*) Above a critical frequency (f_c), the 6-μm microspheres roll continuously along the top channel surface without getting trapped.

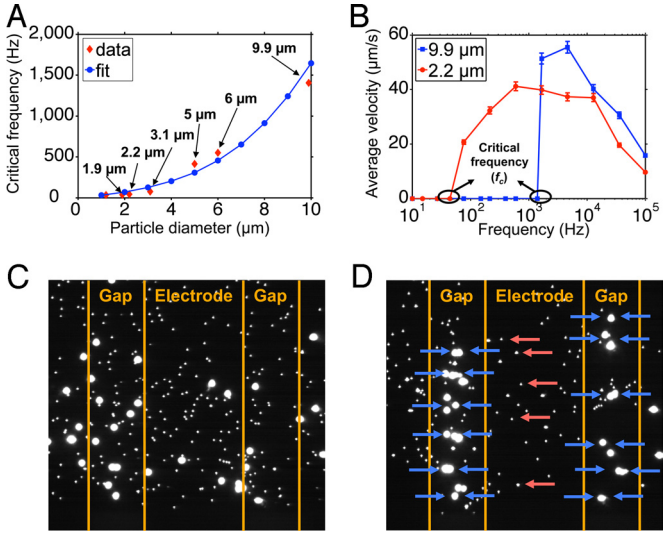

Fig. 4. Frequency-dependent particle separation. (*A*) Particle size dependence of critical frequency (f_c). Discrete f_c values for different diameters of particles enable size-based separation by tuning to the right frequency. Solid curve corresponds to the simulation result with a slip factor of 1 and a particle-wall gap of 1 nm. (*B*) Average manipulation speed as a function of input frequency for two different particle sizes; 2.2- and 9.9-μm particles can be separated at 400 Hz (see Movie S4). (*C*) Fluorescent microscopy image from a section of the microfluidic channel containing 2.2- and 9.9-μm microspheres randomly dispersed within the channel right before the excitation. Vertical lines indicate electrode borders. (*D*) Snapshot of the channel from the same location as in *C* 45 s after the excitation (6 A peak to peak, 400 Hz) is turned on. The 9.9-μm particles quickly localize within the nearest spacing between electrodes, whereas 97% of the 2.2-μm microspheres continuously travel from right to left without being trapped. Almost all of the smaller microspheres within the field of view in *D* have entered from the right as a fresh batch.

quency to separate particle mixtures with more than two distinct sizes. One could also create an electrode pattern with a gradually increasing gap to sort particles based on size (Fig. S1*C*). In this context, we observed that small nonuniformities in actual electrode spacing (caused by fabrication) partly determined the resolution of separation, defined as the minimum size difference in particles that can still be separated with high efficiency (e.g., >90%). Given a range of particle sizes, this resolution of separation is directly related to the difference in the corresponding critical frequencies; under ideal conditions (i.e., perfectly controlled electrode gaps and a very dilute cell concentration), the resolution of separation could be arbitrarily small. However, critical frequencies tend to show slight local variations around each nonuniform electrode gap. As depicted in Fig. 4*A*, the ideal critical frequency depends nonlinearly on the particle radius; hence, a 1-μm difference in diameter between 9- and 10-μm microspheres is easier to resolve (with slight random variations in electrode spacing) than one between 1- and 2-μm particles. Ultimately, the resolution of separation that was achieved in our experiments was $\approx$1 μm for particles 2 μm or larger.

Experiments with Live Cells

Once the physical behavior of the ferromicrofluidic platform was characterized, we conducted manipulation and separation experiments with live human red blood cells and bacteria to demonstrate the utility and practicality of our ferromicrofluidic devices for biomedical applications. Red blood cells and *Escherichia coli* bacteria [K12 strain (32)] were stained with a green fluorescent marker and mixed before suspension in ferrofluid (see *SI Appendix* for sample preparation). The average velocity for cells and bacteria within the channel was measured with 6 A of peak-to-peak current amplitude for frequencies from 10 Hz to 100 kHz. The critical frequencies for cells and bacteria were found to be 215 and 77 Hz, respectively. These f_c values are somewhat lower than those found for comparably sized polystyrene microspheres, because of a combination of compliant shapes and nonspherical geometries that lead to increased difficulty of rolling along the channel roof. Moreover, bacteria

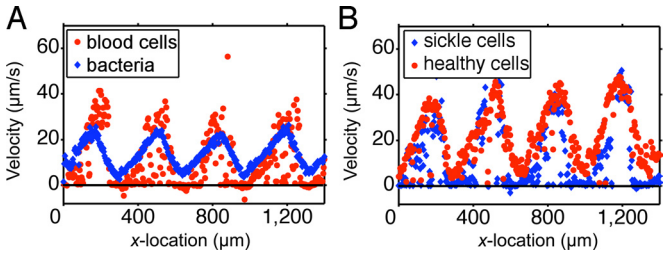

Fig. 5. Cellular separation experiments with bacteria and blood cells. (*A*) Spatial distribution of *x*-velocities at 200 Hz in a sample containing *E. coli* bacteria and red blood cells. At this frequency, most red blood cells are trapped between the electrodes (indicated by their zero local speeds), whereas *E. coli* can slowly but continuously move through that region. Fluctuations in the red blood cell data are statistical in nature, as explained in *Experiments with Live Cells*. (*B*) Sickle cell separation. Sickle cells, which have an elongated shape and altered elasticity compared with normal red blood cells, are trapped and concentrated between the electrodes, whereas the healthy cells are still able to circulate within the microfluidic channel at 300Hz. Electrode spacing of the device in *A* is different from that in *B*, resulting in different f_cs for red blood cells within each channel.

and cells, with their complex surface chemistries, interacted with the PDMS channel more strongly (resulting in more prevalent cellular attachment) than the bare microspheres, indicating potentially higher effective kinetic friction coefficients between the cells and the PDMS surface. Fig. 5*A* depicts the spatially averaged linear velocity of cells and bacteria along the channel for an excitation frequency of 200 Hz. The smaller *E. coli* moved continuously along the channel (velocity points in Fig. 5*A* do not cross zero) and eventually left the observation window, whereas blood cells were localized between electrodes (velocity points reach zero; see Movie S5). Note that the larger variation observable in the red blood cell data of Fig. 5*A* stems from a statistical fluctuation: there are only a few red blood cells that passed through a given *x*-location during the observation window, and their nonspherical shapes mean that each cell would be at a random angular orientation (and slightly different instantaneous velocity) as it rolled down the channel at that location. Bacteria, although varying in length and nonspherical, had enough numbers (several hundred through a given *x*-location) to result in good average statistics. In the end, ≈6,750 of the 7,050 *E. coli* bacteria initially present within the field of view of the sample were cleared (95.7% separation efficiency) within 45 s. Of the 1,018 red blood cells initially present, 954 were trapped, corresponding to a trapping efficiency of 93.7% and cell purity of 76.1%.

In a different experiment, we separated healthy red blood cells from those afflicted with sickle cell anemia by exploiting the shape and elasticity differences between them (Fig. 5*B*). A blood sample containing approximately a 4:1 ratio of healthy-to-sickle red blood cells was added to the ferrofluid and introduced into the microchannel. At 300 Hz, sickle cells were trapped, whereas the healthy blood cells were cleared continuously from the channel (fluctuations in each dataset depicted in Fig. 5*B* are statistical in nature). In a sample initially containing ≈501 healthy red blood cells and 145 sickle cells, 300 healthy cells were cleared, whereas 109 sickle cells were trapped. Assuming that the goal is to clear the sample from sickle cells, these numbers correspond to a separation efficiency of 75.2% (109 of 145 sickle cells were separated from healthy ones) and a healthy cell purity of 89.3% (300 healthy cells and 36 sickle cells were cleared).

Discussion

The results presented above reveal the potential of ferromicrofluidics in significantly reducing incubation times and increasing diagnostic sensitivity in cellular assays through rapid separation and selective delivery of target cells to sensor arrays. Although manipulation and separation of microparticles and live cells within microfluidic devices is also possible through established techniques (such as DEP and magnetic label-based methods), the ferromicrofluidic approach that we introduce here offers certain attractive advantages over these existing methods. With this ferromicrofluidic approach, target cells can be concentrated, trapped, localized, or simply directed toward sensor surfaces efficiently, rapidly, and in a label-free fashion. The biocompatible ferrofluid used in this study can sustain live blood cells for several hours without deterioration in physical properties, allowing extended examination of the target sample.

Combined with a simple photodiode, ferromicrofluidic separation of cells could eventually enable a rapid, automated, and disposable blood assay that counts and estimates the concentration of target cells (whether bacteria or sickle cells) within 1 min, without the need for a microscope, pumps, or lengthy sample preparation steps. It is also conceivable that the same phenomenon could eventually be used to selectively concentrate rare cells, such as circulating tumor cells in blood samples, by exploiting their below normal Young's modulus (33). Applied in this manner, ferromicrofluidics could help boost the detection sensitivity of existing cellular assays.

In summary, we have developed a cellular manipulation and separation platform using biocompatible ferrofluids within low-cost microfluidic devices. We have demonstrated highly efficient particle separation that is achievable in <1 min. As an example, we have demonstrated that bacteria can be separated from live blood cells. We have also applied the same ferromicrofluidic platform to the separation of sickle cells from healthy red blood cells. Work continues on combining ferromicrofluidic particle manipulation with continuous flow within the device channel. In the case of a flow-based device, separation would be most easily achieved with particle manipulation perpendicular to the flow direction. We note that through varying electrode geometry and input excitation frequency these devices could be tailored for different size ranges of particles and cells. Together with control of microchannel surface chemistry, they can be integrated within lab-on-a-chip sensors and diagnostic systems to direct target cells toward active regions. In this manner, ferromicrofluidics could help to significantly reduce incubation times and increase the practical detection sensitivities achieved in existing sensors and diagnostic platforms.

ACKNOWLEDGMENTS. We thank Tarek Fadel and Tarek Fahmy for help with cell viability tests; Jason Hoffman for help with superconducting quantum interference device measurements; and Kaya Bilguvar and Murat Gunel for help with blood sample collection. This work was supported in part by grants from the National Science Foundation, the National Institutes of Health, and the Yale Institute for Nanoscience and Quantum Engineering.

1. Dittrich PS, Manz A (2006) Lab-on-a-chip: Microfluidics in drug discovery. *Nat Rev Drug Discovery* 5:210–218.
2. Beyor N, Seo TS, Liu P, Mathies RA (2008) Immunomagnetic bead-based cell concentration microdevice for dilute pathogen detection. *Biomed Microdevices* 10:909–917.
3. Kamei T, et al. (2005) Microfluidic genetic analysis with an integrated a-Si:H detector. *Biomed Microdevices* 7:147–152.
4. Cheong KH, et al. (2008) Gold nanoparticles for one-step DNA extraction and real-time PCR of pathogens in a single chamber. *Lab Chip* 8:810–813.
5. Ashkin A, Dziedzic JM, Yamane T (1987) Optical trapping and manipulation of single cells using infrared laser beams. *Nature* 330:769–771.
6. Chiou PY, Ohta AT, Wu MC (2005) Massively parallel manipulation of single cells and microparticles using optical images. *Nature* 436:370–372.
7. Hughes MP (2002) Strategies for dielectrophoretic separation in laboratory-on-a-chip systems. *Electrophoresis* 23:2569–2582.
8. Lee CS, Lee H, Westervelt RM (2001) Microelectromagnets for the control of magnetic nanoparticles. *Appl Phys Lett* 79:3308–3310.
9. Yan J, Skoko D, Marko JF (2004) Near-field-magnetic-tweezer manipulation of single DNA molecules. *Phys Rev E* 70:011905.
10. Davis JA, et al. (2006) Deterministic hydrodynamics: Taking blood apart. *Proc Natl Acad Sci USA* 103:14779–14784.

11. Dufresne ER, Grier DG (1998) Optical tweezer arrays and optical substrates created with diffractive optics. *Rev Sci Instrum* 69:1974–1977.
12. Kremser L, Blaas D, Kenndler E (2004) Capillary electrophoresis of biological particles: Viruses, bacteria, and eukaryotic cells. *Electrophoresis* 25:2282–2291.
13. Cabrera CR, Yager P (2001) Continuous concentration of bacteria in a microfluidic flow cell using electrokinetic techniques. *Electrophoresis* 22:355–362.
14. Liu Y, et al. (1995) Evidence for localized cell heating induced by infrared optical tweezers. *Biophys J* 68:2137–2144.
15. Ashkin A, Dziedzic JM (1987) Optical trapping and manipulation of viruses and bacteria. *Science* 235:1517–1520.
16. Applegate RW, et al. (2004) Optical trapping, manipulation, and sorting of cells and colloids in microfluidic systems with diode laser bars. *Optical Express* 12:4390–4398.
17. Pethig R, Markx GH (1997) Applications of dielectrophoresis in biotechnology. *Trends Biotechnol* 15:426–432.
18. Menachery A, Pethig R (2005) Controlling cell destruction using dielectrophoretic forces. *NanoBiotechnology* 152:145–149.
19. Müller, et al. (2003) The potential of dielectrophoresis for single-cell experiments. *IEEE Eng Biol Med Mag* 22:51–61.
20. Sebastian A, Buckle AM, Markx GH (2006) Formation of multilayer aggregates of mammalian cells by dielectrophoresis. *J Micromech Microeng* 16:1769–1777.
21. Gijs MAM (2004) Magnetic bead handling on-chip: New opportunities for analytical applications. *Microfluidics Nanofluidics* 1:22–40.
22. Kashevsky BE (1997) Nonmagnetic particles in magnetic fluid: Reversal dynamics under rotating field. *Phys Fluids* 9:1811–1818.
23. Rosensweig RE (1997) *Ferrohydrodynamics* (Dover, New York).
24. Odenbach S (2002) *Ferrofluids: Magnetically Controllable Fluids and Their Applications* (Springer, New York).
25. Yellen BB, Hovorka O, Friedman G (2005) Arranging matter by magnetic nanoparticle assemblers. *Proc Natl Acad Sci USA* 102:8860–8864.
26. Kose AR, Fischer B, Koser H (2008) Toward ferro-microfluidics for effective and rapid cellular manipulation and sorting. *Proceedings of the 3rd IEEE International Conference on Nano/Micro Engineered and Molecular Systems* (IEEE, Los Alamitos, CA), pp 903–906.
27. Mao L, Koser H (2006) Toward ferrofluidics for μ-TAS and lab on-a-chip applications. *Nanotechnology* 17:34–47.
28. Kim EH, Lee HS, Kwak BK, Kim B-K (2005) Synthesis of ferrofluid with magnetic nanoparticles by sonochemical method for MRI contrast agent. *J Magn Magn Mater* 289:328–330.
29. Scherer C, Figueiredo Neto AM (2005) Ferrofluids: Properties and applications. *Brazilian J Phys* 45:718–727.
30. Bautista, et al. (2004) Comparative study of ferrofluids based on dextran-coated iron oxide and metal nanoparticles for contrast agents in magnetic resonance imaging. *Nanotechnology* 15:S154–S159.
31. Fischer B, et al. (2008) Ferro-microfluidic device for pathogen detection. *Proceedings of the 3rd IEEE International Conference on Nano/Micro Engineered and Molecular Systems* (IEEE, Los Alamitos, CA), pp 907–910.
32. Blattner FR, et al. (1997) The complete genome sequence of *Escherichia coli* K-12. *Science* 277:1453–1474.
33. Lekka M, et al. (1999) Elasticity of normal and cancerous human bladder cells studied by scanning force microscopy. *Eur Biophys J* 28:312–316.